Forensic Imaging 44 (2026) 200667

Contents lists available at ScienceDirect

Forensic Imaging

journal homepage: www.sciencedirect.com/journal/forensic-imaging

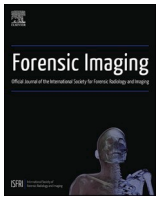

Validating the morphology of 3D-printed cranial projectile trauma as a skeletal alternative for utilisation in a court of law

Claudia Ibáñez Martín [a,b,*], Ericka Noelle L'Abbé [b], Pieter Daniël de Wet [b], Alison Fany Ridel [b]

[a] Department of Forensic Science, Faculty of Science, University of Amsterdam, Science Park 904, 1098 XH Amsterdam, the Netherlands
[b] Department of Anatomy, Faculty of Health Sciences, University of Pretoria, Private Bag X323, Arcadia, 0007, Pretoria, South Africa

ARTICLE INFO

Keywords:
3D-printing
Projectile injury
Micro-XCT
Morphology validation
Forensic anthropology
Skeletal trauma analysis

ABSTRACT

Forensic anthropology has become crucial for global cases involving firearm-related injuries. Although skeletal evidence is valuable, its presentation in court may re-traumatise families or bias reactions, influencing the verdict. To mitigate these risks, the adoption of 3D printing technologies in court has increased, allowing the handling of human remains without the drawbacks of presenting biological evidence. This study aimed to validate 3D-printed skeletal technologies as alternatives for courtroom evidence, focusing on cranial bullet defects through 3D topographical analysis and investigating the accuracy of 3D-printed skeletal models. Samples were scanned using micro-focus X-ray computed tomography; their 3D meshes were generated, 3D printed using powder Selective Laser Sintering, resin Stereolithography, and polylactic acid (PLA) filament Fused Deposition Modelling technologies, and scanned again. The reference and 3D print meshes were aligned, and a colour map allowed visual inspection of morphological discrepancies of up to 1 mm (0 mm shown in blue, 1 mm in red). Powder-based prints exhibited the highest accuracy for representing crania, predominantly coloured dark blue (0 mm). PLA filament prints were accurate for examining smaller cranial surfaces (mostly 0 mm), whereas resin prints were the least accurate for crania (mostly 0.5-1 mm). 3D-printed skeletal material can be utilised in legal settings with a colour map elucidating discrepancies. While powder-based prints are preferred, other materials may better suit specific applications. Further research should evaluate the impact of 3D prints on judicial decision-making and refine 3D printing techniques for forensic anthropology.

1. Introduction

Approximately 85 % of global firearms are held by civilians, significantly heightening the risk of firearm-related homicides worldwide [1]. Forensic scientists, such as ballistic experts, forensic pathologists, and forensic anthropologists, need to explain to a judge or a jury their findings related to the interpretation of ballistic injuries to soft tissue, bone, and/or inanimate material surrounding a body. In many instances, this may include the use of a 3D model of a bone(s) or a replica of a crime scene.

Presenting the original bone with traumatic injury in a courtroom or classroom poses several challenges. Students might inadvertently damage skeletal material during handling or feel apprehensive about working with it, especially when they understand that the bones were associated with violent crimes. In the courtroom, the bone may be compromised or damaged during transportation, handling, or presentation [2]. Such inadvertent damage to bone could also introduce bias, potentially leading to a misinterpretation of evidence. Additionally, demonstrative skeletal evidence, such as graphic images or the actual bone, could negatively influence jurors and judges and could create bias against the defendant [3]. The explicit nature of a crime scene or the display of skeletal elements in court may also cause emotional distress for the victim's family and other participants [4].

Three-dimensional prints have the potential to overcome these by providing visually intuitive, detailed, and accurate representations of evidence, enhancing understanding in both courtrooms and teaching environments. Advances in technology have made 3D bone models increasingly accessible and potentially useful as transformative tools for explaining and interpreting forensic findings, such as bone trauma [5,6]. However, questions remain about how accurately these models can replicate real bones and skeletal trauma. When validated, 3D models and prints could address critical gaps in forensic science education and

* Corresponding author.
E-mail addresses: claudia.ibanezmartin1@gmail.com (C. Ibáñez Martín), Ericka.Labbe@up.ac.za (E.N. L'Abbé), u04510462@tuks.co.za (P.D. de Wet), alison.ridel@up.ac.za (A.F. Ridel).

https://doi.org/10.1016/j.fri.2025.200667

Available online 17 December 2025

practice by providing accessible, standardised representations of bone trauma. Their potential extends to courtrooms and classrooms, where they can serve as valuable tools to clarify complex findings for non-specialists [4,7].

Research highlights the advantages of 3D-printed models in improving information retention and maintaining attention in legal settings, leading to more objective and informed decision-making as these models are also more comprehensible and less emotionally charged than other forms of evidence presentation [5,4,7]. For instance, 3D-printed skeletal models can replicate original bones while allowing modifications in colour and size to reduce their human-like appearance, thereby minimising bias by decreasing the emotional effect on the involved parties and preserving the integrity of the evidence [8,9]. While 3D-printed skeletal materials have been successfully used in courts in England and Wales for cases involving cranial wounds and dismemberments [10], their application in other regions remains largely unexplored.

The use of 3D prints can enhance visual understanding of injuries, offering a valid and effective tool for both courtroom presentations and educational purposes [11,4,7]. However, research is required to assess the accuracy of these models compared to the original bones they replicate. Understanding the accuracy of 3D prints to the original material is crucial for ensuring their reliability in forensic contexts and education. The purpose of this research is to validate, with the use of distance colour map analysis, the use of 3D-printed gunshot wounds in skulls and crania as a reliable alternative to the actual bone.

2. Materials and methods

2.1. Samples and ethical approval

The samples were selected from the forensic archives of the Department of Anatomy at the University of Pretoria, South Africa. These archives include a total of 720 analysed cold cases, including 250 females and 449 males, among which 25 cases exhibit gunshot wounds (GSW) or projectile trauma. The study sample consisted of three complete skulls and two complete crania with single or multiple GSW, and two cranial sections with entry defects (Table 1). All cases have been anonymised. Ethical approval was granted by the Human Research Ethics Committee (HREC) of the Faculty of Health Sciences at the University of Pretoria and by the forensic archives of the Department of Anatomy at the University of Pretoria (200/2024).

2.2. Acquisition and reconstruction of scans

The original skulls, crania, and cranial sections, along with their 3D prints, were scanned at the South African Nuclear Energy Corporation (NECSA) using a Nikon XTH 225 L microfocus X-ray Computer Tomography (micro-XCT) system (Nikon Metrology), which was used due to its higher accuracy compared to other scanning technologies such as Computer Tomography or Magnetic Resonance Imaging, making it ideal for forensic 3D models [12]. This system operates within a 30 to 225 kV voltage range and a beam current range from 0 to 1 mA, with a maximum power capacity of 30 W. The X-ray tube has a spot size between 0.001 and 0.003 mm. For the scanning process, the beam energy was set to 100 kV and the beam current to 100 μA, as configured using the Inspect-X software (Nikon Metrology). The scanning resolution (effective pixel size) for the 3D prints was adjusted to match that of the original specimens based on visual assessment. During the scanning procedure, the samples were secured on a sample manipulator within the micro-focus X-ray chamber to ensure stability and prevent movement.

The resulting scans were processed in CT Pro 3D software (version XT 4.4.3) (Nikon Metrology), where they were adjusted in the x, y, and z planes to facilitate 3D modelling. During the reconstruction process, noise was filtered out and image quality was enhanced. These image stacks were saved in .tiff format for further processing. This raw data file was imported into visualisation software for subsequent segmentation.

Table 1
Samples used in this study, including the resolution used for the Micro X-ray Computed Tomography (Micro-XCT) scans and prints and during the segmentation of the scans. The list also includes the material(s) used for the sample prints: Powder, Resin, or Polylactic Acid (PLA) filament.

Sample name	Skeletal element	Resolution (mm)	Printing material
CS-01	Cranium (occipital section)	0.055	PLA filament
CS-02	Cranium (occipital section)	0.061	PLA filament
SK-01	Skull	0.119	Powder PLA filament Resin
CR-01	Cranium	0.108	Powder Resin
SK-02	Skull	0.127	Powder PLA filament
SK-03	Skull	0.100	Powder
CR-02	Cranium	0.119	PLA filament

2.3. 3D printing technology

This study utilised three 3D printing technologies. The first was Fused Deposition Modelling (FDM) using Polylactic Acid (PLA) filament, which involves the fusion of filaments added layer by layer according to the 3D model [13].

The second technology employed was Stereolithography (SLA) 3D printing using liquid resin (Formlabs White V4 photopolymer resin), a form of vat polymerisation. This process cures selective areas within a vat of liquid resin using UV light. During resin printing, the platform ascends after each layer is cured, whereas in PLA filament printing, the platform remains stationary, and the nozzle ascends instead. Once a resin print is complete, it must undergo additional curing in a UV chamber to finalise the process [8].

The final technology used was Selective Laser Sintering (SLS) through powder bed fusion. This technique fuses metal powders using a laser [8]. Both PLA filament and resin prints require supports to stabilise certain areas of the print, such as overhangs and bridges, which must be manually removed after printing and, in the case of resin prints, post-curing [8,14]. In contrast, powder printing does not require support, as the surrounding powder provides sufficient stability during the process.

The resolution of these printers can vary. Specifically, SLA printers can produce walls as thin as 0.2 mm, thinner than FDM printers (0.8 mm) and SLS printers (0.3 mm for horizontal structures). Regarding the duration of the printing process, FDM printers typically take the longest, followed by SLS printers and SLA printers. Cost-wise, SLS prints tend to be the most expensive to obtain, followed by SLA prints, with FDM prints being the least costly when considering the overall costs of printers and materials used [15].

2.4. Image segmentation

The obtained scans were first adjusted for contrast and brightness using ImageJ software [16], processing them as image sequences. Following this, the scans were imported into Amira-Avizo 2019.3 software (Thermo Fisher Scientific, Inc.) for further processing and 3D model generation. The segmentation process enabled the extraction of skeletal areas by segmenting between the bone (referred to as “Bone”) and the surrounding area (referred to as “Air”) based on their intensity differences (grey levels). The “Air” was removed to isolate and model the “Bone” effectively. The *Edit New Label Field* module was used to manually set segmentation thresholds, employing the “Half Maximum

Height" (HMH) quantitative iterative thresholding approach [17]. After refining the 3D model and removing noise, the surface was extracted and saved in both .ply and .stl formats. Manual adjustments finalised the segmentation, and the 3D models of the bones were generated and exported in .stl format. In this paper, the 3D model created from the original bone scan is referred to as the *reference mesh*, while the 3D model(s) produced from the scan(s) of subsequent print(s) are referred to as the *3D print mesh(es)*.

2.5. Alignment

The reference meshes and their 3D print meshes were aligned using MeVisLab (version 2.7.1) software (MeVis Medical Solutions AG) using six manually placed anatomical landmarks on the reference meshes to ensure accurate positioning within the same 3D space as the 3D print meshes. These landmarks included the auricularia, the glabella, the rhinion, the nasospinale, and the alveolare (Table 2).

When aligning the cranial section meshes, six landmarks were placed in identifiable areas chosen during the analysis, such as on the edges of the defect and of the sections.

The initialisation procedure was performed using the WEMMarker-Initialization module in MeVisLab (version 2.7.1) (MeVis Medical Solutions AG), which involved rotating and translating the surfaces to bring them into close proximity with each other. This procedure aligns the surfaces into a common coordinate system by repositioning the floating surface into the coordinate space of the target surface through affine transformations. For this study, initialisation was manually executed by placing the abovementioned anatomical landmarks on both floating (3D print mesh) and target (reference mesh) surfaces. This manual landmark-based approach enabled interactive rotation and translation, ensuring accurate initial alignment. The quality of the subsequent non-rigid surface registration used for topographical colour map analysis depended on the precision of this initial alignment procedure.

2.6. Topographical analysis using non-rigid registration and colour mapping

To enable the visualisation of geometric discrepancies, 3D reconstructions of the reference meshes and their corresponding 3D print meshes were loaded on Amira-Avizo 2019.3 software (Thermo Fisher Scientific, Inc.) for non-rigid surface registration and alignment within a common coordinate system. Non-rigid registration aligns the reference and 3D print meshes by permitting local deformations, allowing a more precise alignment of morphological features. This was performed using the *Geometric Transform* module in Amira-Avizo 2019.3 (Thermo Fisher Scientific, Inc.) and selecting the option "rigid + uniform" under *Align Surfaces*. The iterated closest points algorithm, executed over 15 iterations, was employed to minimise the distance between corresponding points of the micro-XCT and 3D prints. Subsequently, the surface distance between the 3D prints and the reference meshes was calculated, with discrepancies not exceeding 1 mm. The discrepancies were visualised using the colour map module in Amira-Avizo 2019.3 (Thermo Fisher Scientific, Inc.), which produced a colour map depicting geometric discrepancies, ranging from blue (indicating minimal discrepancies, or 0 mm) to red (indicating maximal discrepancies, or $\geq$ 1 mm). This colour map facilitated the precise identification of significant morphological differences between the reference meshes and their 3D print meshes. No quantitative measurements were performed. Instead, morphological discrepancies were evaluated qualitatively by visually assessing each colour map. Comparisons were conducted for each skeletal sample and its respective 3D print. Additionally, for samples SK-01, CR-01, and SK-02, comparisons were made between the original bones and their 3D prints created from various materials: SK-01 was printed in powder, resin, and PLA filament; CR-01 in powder and resin; and SK-02 in powder and PLA filament.

Table 2
Landmarks used in this study, including their definitions and placement order [18].

Landmark	Landmark type	Definition	Placement order
Auriculare	Bilateral	On the zygomatic root, vertically above the centre of the external auditory meatus.	1 (right), 2 (left)
Glabella	Medial	Most projecting anterior median point on lower edge of the frontal bone, on the brow ridge, in between the superciliary.	3
Rhinion	Medial	Most rostral (end) point on the internasal suture. Cannot be determined accurately if nasal bones are broken distally.	4
Nasospinale	Medial	The point where a line drawn between the inferior most points of the nasal aperture crosses the median plane. Note that this point is not necessarily at the tip of the nasal spine.	5
Alveolare	Medial	Median point at the inferior tip of the bony septum between the upper central incisors. Equivalent to Infradentale superius.	6

2.7. Intra- and inter-operator reproducibility

Intra- and inter-operator reproducibility testing was performed on a subsample of five specimens to assess the reliability of colour map analysis. This involved repeated alignment based on manually placed anatomical landmarks (used only for alignment, not for reproducibility testing) and subsequent colour map analysis by different operators (inter-reproducibility) and by the same operator (intra-reproducibility).

3. Results

3.1. FDM printing technology with PLA

3.1.1. FDM printing technology with PLA: visual presentation of the prints

The PLA filament prints were white in colour (PLA was light ivory from Form Futura). The filament was perceptible to the touch, which was also occasionally the case for areas of support adhesion, like the resin prints. The accuracy of the 3D prints was generally consistent with the reference bones upon visual comparison. However, several defects were observed, including layer adhesion failures, commonly called "spaghetti defects" due to their appearance [19]. Other issues included visible support structures, gaps between filaments, flattened regions, and areas of material loss.

3.1.2. PLA printing technology: topographical colour map analysis

The PLA filament prints of the two cranial sections exhibited minimal discrepancies when compared to their reference meshes. Colour maps predominantly displayed dark blue, with only occasional light blue or blue-green areas noted near the edges of the skeletal structures, such as around the internal occipital crest in sample CS-01 and the external edge of the cut on the left side of the external occipital protuberance in sample CS-02. Some light blue-green specks were also observed alongside the filament lines added during the printing process. Both entrance defects on CS-01 and CS-02 displayed discrepancies of 0 mm or values very close to 0 mm based on their colour maps.

The PLA filament samples included two skulls and one cranium, with no specific similarities identified upon analysis of the colour maps. For sample SK-01, the colour map showed a predominantly red left side, with a mixture of red, green, and dark blue on the right side. The posterior aspect of the cranium exhibited more variation than the

viscerocranium (Fig. 1, 1a and b). Sample CR-02 displayed a primarily dark blue colour on the viscerocranium, with a small red area near the bregma and a smaller circle under the left orbit, indicating a hole present in the print but absent on the bone (Fig. 1, 2a). Sample SK-02 showed a predominantly red viscerocranium, with small blue and green areas above the nasal cavity and on the maxilla. A green-to-blue gradient was observed towards the superior left side of the skull (Fig. 1, 3a). Specifically, the posterior region of SK-02 exhibited green on the left parietal, dark blue on the right parietal, and green again further along the right parietal, while the sutures were mainly dark blue (Fig. 1, 3b). In contrast, sample CR-02 revealed visible triangular patterns despite being simplified similarly to other samples, with greener areas and some red specks observed on the posterior aspect, particularly around the right parietal and left side of the occipital. The sutures, although mainly dark blue, showed some green areas (Fig. 1, 2a and b). Sample SK-01 displayed a continuation of the printing pattern from the right side of the viscerocranium, with parallel lines, a red central area on the posterior region of the skull, and a small dark blue area on the right parietal (Fig. 1, 1b).

For sample SK-01, the right side maintained the previously observed linear pattern, most prominently on the cranial vault and mandible, with a smaller area affected on the right side of the maxilla (Fig. 2, 1c). In contrast, CR-02 displayed a varied colour map on the right side, including dark blue, light blue, green, yellow, and red patches. The most significant discrepancies were found around the radiating fractures in the temporal and parietal regions (Fig. 2, 2c).

The right side of sample SK-02 predominantly exhibited red, except for the upper portion of the right parietal bone (Fig. 2, 3c). The left profiles of the three samples generally showed slightly better accuracy than the right profiles. For SK-02, the dark blue pattern extended from the frontal to the occipital bone, with additional dark blue and green areas present on the zygomatic process, nasal bones, ascending ramus of the mandible, and maxilla (Fig. 2, 3d).

The left profile of CR-02 was predominantly dark and light blue, though it included a green area on the temporal bone and some red patches around the edges of the entry defect and the mastoid bone (Fig. 2, 2d). Conversely, SK-01 exhibited larger red areas with a reduction in the linear pattern and showed some patchy areas of dark blue, green, and scattered red. This less discrepant area was clearly demarcated on the parietal bone, sphenoid bone, and parts of the temporal bone (Fig. 2, 1d).

Upon analysing the colour maps from the superior view of the crania, no consistent pattern emerged across the samples. Sample SK-01 exhibited a continuation of the less discrepant area seen on the left side of the skull, forming a well-defined red circle encompassing the left parietal and part of the frontal bone (Fig. 3, 1e).

Sample CR-02 displayed a predominantly dark blue top interspersed with green, yellow, and red areas at the anterior and posterior of the cranium. The triangular pattern, which was noted on the right profile, was present but less prominent. Notably, a more heterogeneous area on the superior aspect of the cranium coincided with a defect on the print—a flat region absent on the bone, which appeared less discrepant on the colour map compared to the physical print (Fig. 3, 2e).

In sample SK-02, the previously observed pattern on the colour map was more pronounced, with visible rings anterior to the bregma indicating the presence of excess PLA material from the printing process (Fig. 3, 3e). The inferior view revealed a predominance of red areas for SK-02, light and dark blue for CR-02, without distinct patterns, and uniform red areas for SK-01, with some heterogeneous regions maintaining the linear pattern on the right side of the occipital bone and dark blue areas on the left temporal bone (Fig. 3, 1f, 2f, and 3f).

During the examination of entry defects, the accuracy of the 3D print differed amongst the different colour maps. In sample SK-02, a prominent red outline and red surrounding area were observed around the entry defect above the right orbit on the frontal bone (Fig. 1, 3a). A similar pattern was noted for the entry defect on the left parietal bone of sample SK-01 (Fig. 2, 1d). In contrast, the second entry defect of SK-02, located on the right parietal bone, exhibited a less pronounced discrepancy, with a dark blue outline and predominantly dark blue and green surrounding areas (Fig. 2, 3d). Sample CR-02 displayed an entry defect on the left temporal bone, encircled mostly by green areas, although the upper left quadrant of the defect (superior-frontal) appeared blue. The superior outline of this entry defect and the initiation of radiating fractures towards the occipital and frontal bones were

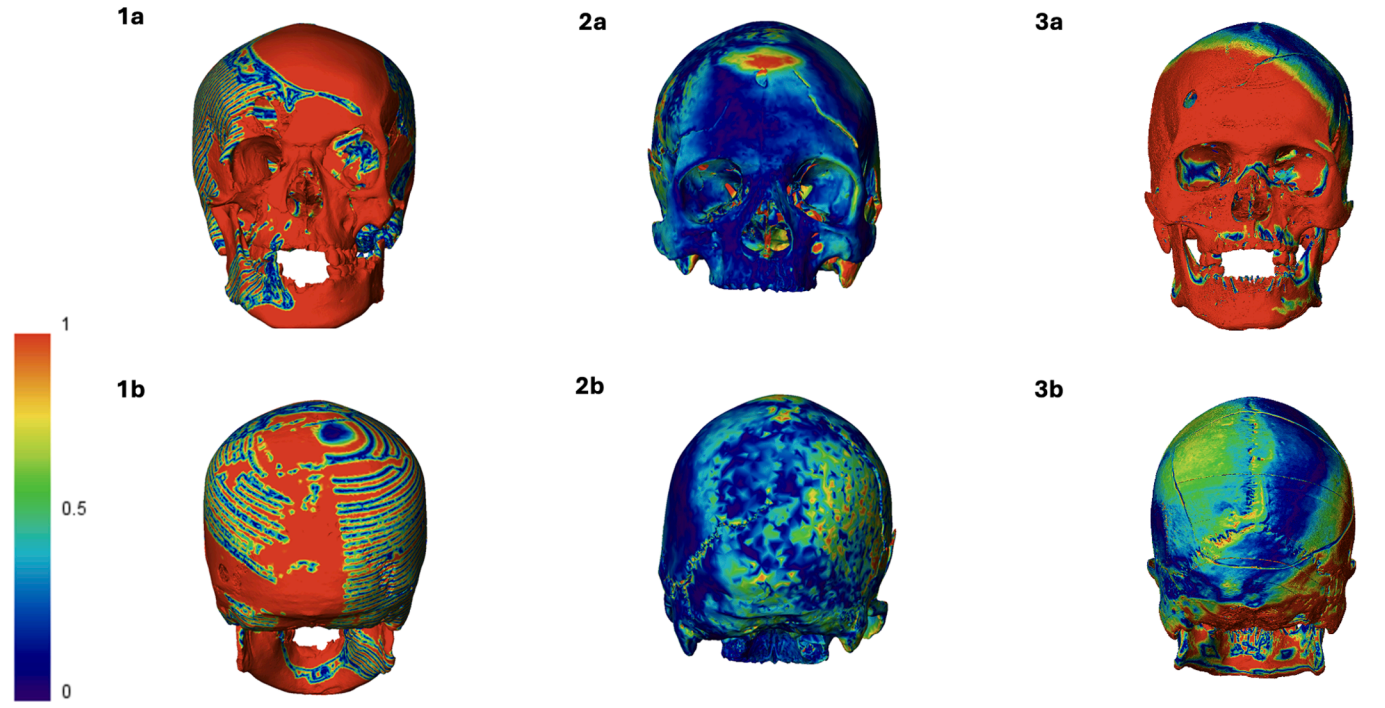

Fig. 1. a) Anterior and b) posterior views of the colour maps displaying the discrepancies between samples 1) SK-01, 2) CR-02, and 3) SK-02 and their respective PLA filament prints. The colour map scale on the left indicates the level of discrepancy shown on the print in millimetres.

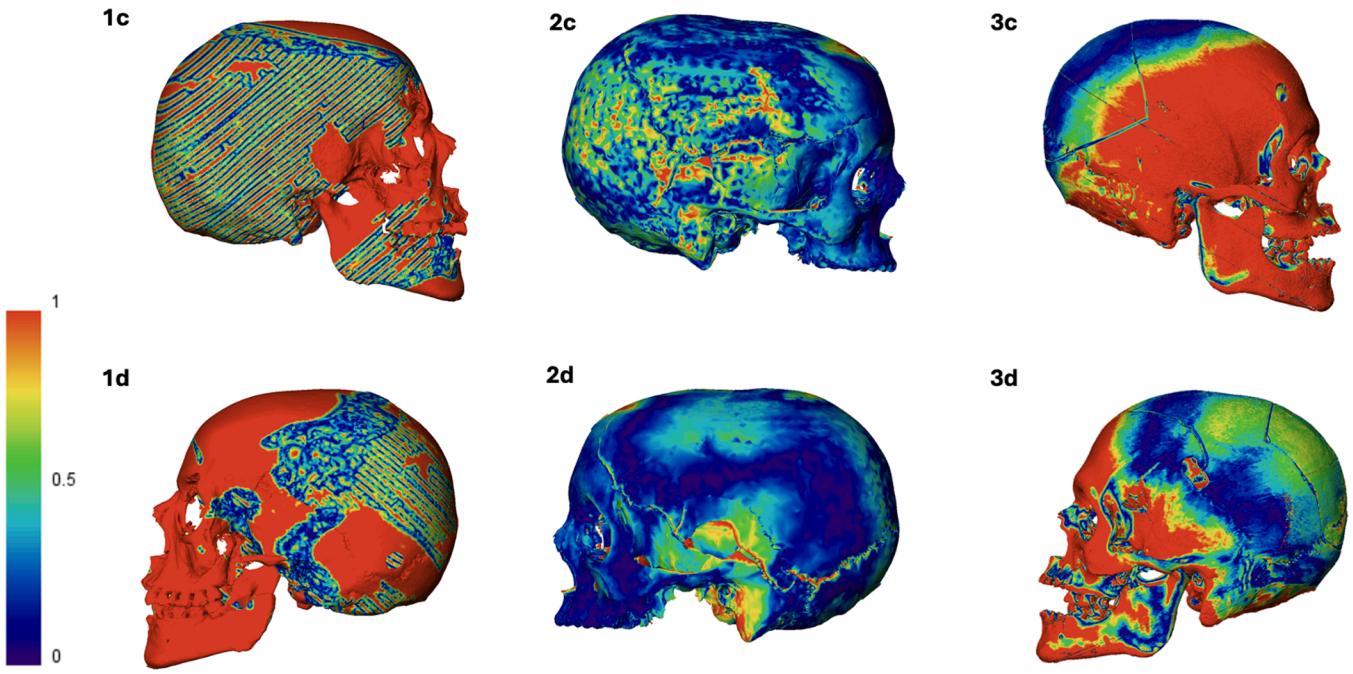

Fig. 2. c) Right and d) left side views of the colour maps displaying the discrepancies between samples 1) SK-01, 2) CR-02, and 3) SK-02 and their respective PLA filament prints. The colour map scale on the left indicates the level of discrepancy shown on the print in millimetres.

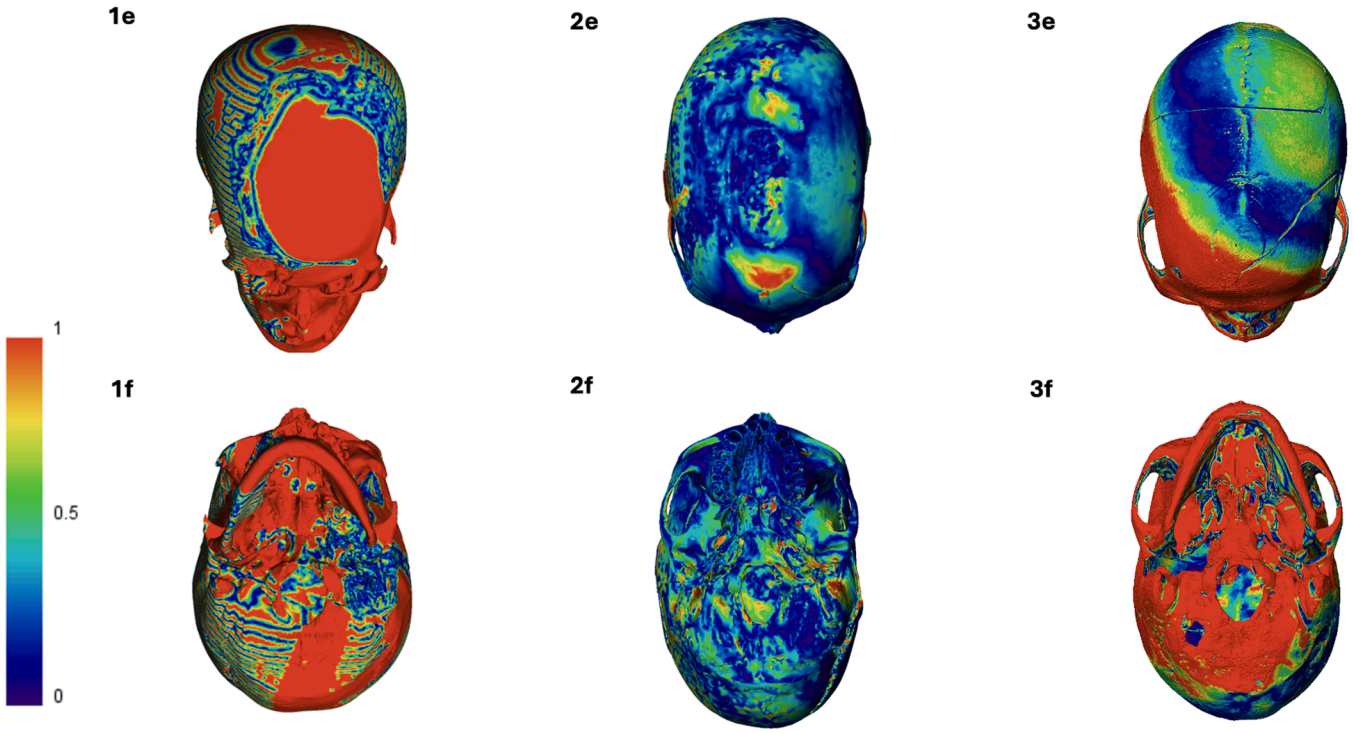

Fig. 3. e) Superior and f) inferior views of the colour maps displaying the discrepancies between samples 1) SK-01, 2) CR-02, and 3) SK-02 and their respective PLA filament prints. The colour map scale on the left indicates the level of discrepancy shown on the print in millimetres.

coloured red (Fig. 2, 2d).

The analysis of exit defects revealed similar findings to those of the entrance defects. SK-02 had an exit defect on the left sphenoid bone, outlined in red and surrounded by a red area at the inferior aspect, with the superior aspect depicted in green on the colour map (Fig. 2, 3d). The second exit defect, located on the right side of the occipital bone, just posterior to the foramen magnum, was also outlined and surrounded by red, with some chipping indicated in green (Fig. 3, 3f). In sample CR-02, the exit defect situated between the right temporal and sphenoid bones was outlined in dark blue. The onset of radiating fractures was marked in red, with the surrounding areas displaying a mix of dark blue, green, yellow, and red (Fig. 2, 2c). Finally, the exit defect in sample SK-01, positioned over the right orbit, exhibited a linear pattern in the superior half and was coloured red in the inferior half (Fig. 1, 1a).

3.2. Resin prints

3.2.1. Resin printing technology: visual presentation of the prints

The resin prints exhibited an off-white hue and a generally smooth surface, although occasional support adhesion areas revealed incomplete support removal. Overall, the prints were largely representative of the sample material, but some defects were noted. For instance, in sample CR-01, the resin print displayed a significant area missing on the right side of the parietal bone, extending to the frontal gunshot wound. A second resin print of the same sample also had a triangular void in this region. Additionally, several resin prints exhibited small drainage holes, which could be confused for foramina (see Fig. 4). Deformation was observed in the same specimen, where the left side of the sagittal suture appeared sunken relative to the corresponding skeletal structure.

3.2.2. Resin printing technology: topographical colour map analysis

Upon examining the viscerocranium of the resin prints for specimens SK-01 and CR-01, several notable observations were made. For sample SK-01, the structural edges—such as those of the orbits, nasal cavity, mental foramen, teeth, and the defect over the right orbit—were delineated in dark blue, while most of the intervening surfaces were coloured in red (Fig. 5, 1a).

In contrast, sample CR-01 exhibited a more distinct colour pattern, with specific structures, including the inferior halves of the orbits and the nasal cavity, outlined in dark blue. The left zygomatic bone showed fewer discrepancies compared to the right, and the frontal bone was fragmented, with each fragment displaying a unique colour pattern rather than a uniform one across the entire bone (Fig. 5, 2a).

When viewed from the posterior view, sample SK-01 predominantly displayed red surfaces, except for areas near the sagittal suture on the right parietal bone and the lambdoid sutures, which were coloured green and dark blue (Fig. 5, 1b). In contrast, sample CR-01 displayed a Y-shaped colour gradient transitioning from dark blue to green and yellow, originating at the parietal bones, intersecting above the lambda, and extending along the right side of the sagittal and right lambdoid sutures (Fig. 5, 2b).

The topographical colour map of the right side of sample SK-01 revealed a dark blue region over the temporal bone, transitioning to a lighter blue near the sphenoid bone. Above this, the colour gradient shifted progressively to green, yellow, and ultimately red across the parietal bone. The mandible predominantly appeared green, except for the menton, which was represented in red (Fig. 6, 1c). In sample CR-01, an intriguing observation was made on the superior portion of the cranial vault. While the physical print did not display this feature, the colour map suggested a symmetrical surface, with the appearance of bullet defects symmetrically positioned in that region. However, the colour maps themselves were not symmetrical. Two prominent dark blue areas were identified, forming curved lines. One of these lines, resembling a Y-shape, originated on the frontal bone, extended across the right parietal and temporal bones, reached the mastoid region, and continued horizontally beneath the zygomatic process, terminating at the maxillary bone (Fig. 6, 2c and 2b).

Fig. 4. Underside of the resin print of sample CR-01 showing the drainage holes circled in red.

On the left side of SK-01, most areas were red, except for the left lambdoid suture, the defect on the parietal bone, and the sphenoid, which were depicted in green and dark blue. A similar pattern was noted on the teeth, and the superior part of the ascending ramus of the mandible and the maxilla appeared yellow (Fig. 6, 1d). On the left side of sample CR-01, another curved line was observed, extending from around the bregma towards the zygomatic process in a linear fashion, including one of the defects, though narrower compared to the right side. The left zygomatic bone was also depicted in dark blue. The remainder of the left profile was largely red, except for the outline of the second defect and a triangular area on the parietal bone, corresponding to a missing section on the print, which was shown in dark blue. This missing section, however, was inaccurately positioned on the colour map (Fig. 6, 2d).

Upon analysing the colour maps from the inferior view, both samples exhibited considerable variability in surface colouration, with the palate and occipital bone displaying the least discrepancies, particularly just posterior to the foramen magnum (Fig. 7). When examined from a superior view of the cranium, sample SK-01 predominantly showed red areas, interspersed with dark blue and green patches around the radiating fractures and on the most dorsal aspect of the right parietal bone (Fig. 7, 1e). In contrast, the colour map for specimen CR-01's superior view also revealed linear bands of dark blue transitioning into green, with interspersed red areas. These red areas were notably present on the posterior part of the left parietal bone, along the right side of the sagittal suture (including the suture itself), and on the right side of the frontal bone. Additionally, a red region was observed across the central fracture on the frontal bone (Fig. 7, 2e).

3.3. Powder prints

3.3.1. Powder printing technology: visual presentation of the prints

The most distinctive characteristic of powder prints, in comparison to other types of prints, was their dark grey colouration and rough texture. When visually assessed against their skeletal counterparts, these prints demonstrated high accuracy, with no significant defects observed.

3.3.2. Powder printing technology: topographical colour map analysis

Upon analysis of the colour maps, distinct differences in accuracy levels emerged when compared to those generated from resin or PLA filament prints. Indeed, the colour maps resulting from the comparison between the reference meshes and the 3D scans from powder prints exhibited a higher prevalence of dark and light blue, indicating a distance close to or equal to 0 mm. In the anterior view, a notable pattern was the increased discrepancy in the teeth compared to other facial features (Fig. 8). This trend was also evident in the zygomatic bones, except in sample CR-01, where the right zygomatic bone appeared dark blue (Fig. 8, 2a), and in sample SK-03, where both zygomatic bones were dark blue (Fig. 8, 4a). All powder-printed samples displayed defects and/or fractures on the frontal bone, except for SK-03. Specifically, sample SK-01 exhibited an exit defect over the right orbit (Fig. 8, 1a),

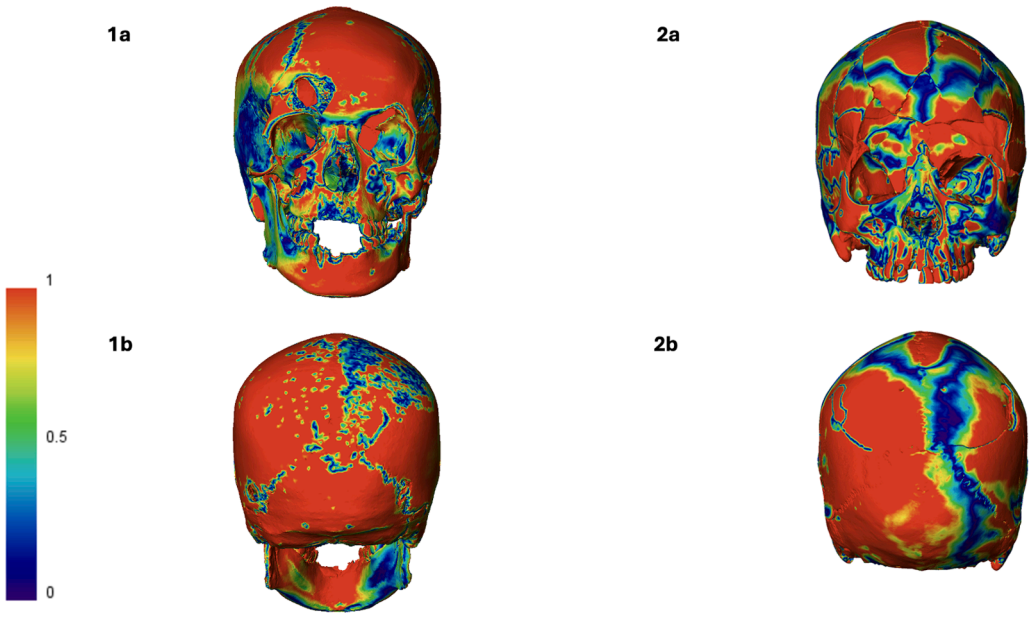

Fig. 5. a) Anterior and b) posterior views of the colour maps displaying the discrepancies between samples 1) SK-01 and 2) CR-01, and their respective resin prints. The colour map scale on the left indicates the level of discrepancy shown on the print in millimetres.

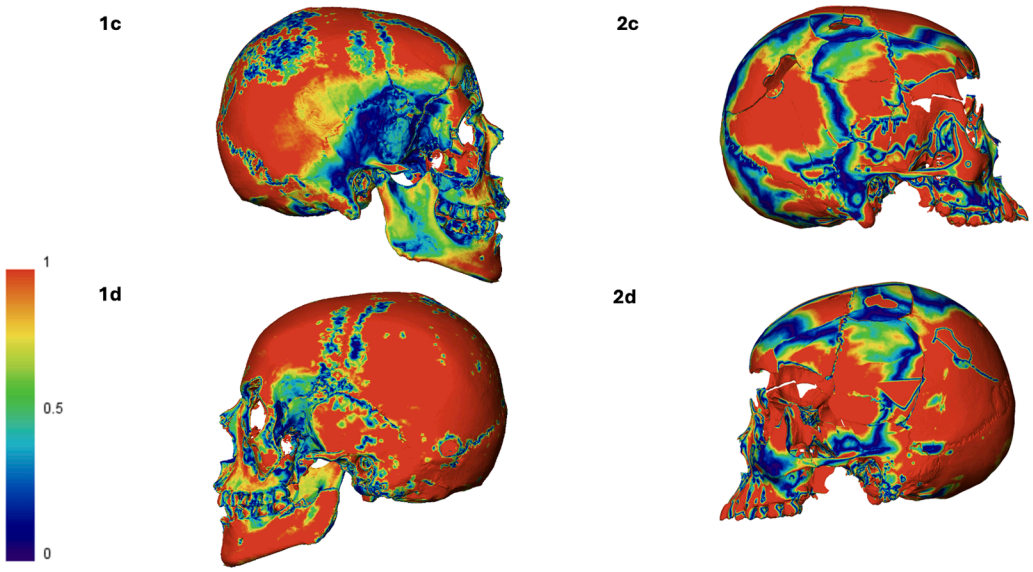

Fig. 6. c) Right and d) left side views of the colour maps displaying the discrepancies between samples 1) SK-01 and 2) CR-01, and their respective resin prints. The colour map scale on the left indicates the level of discrepancy shown on the print in millimetres.

while sample SK-02 displayed an entry defect over the right orbit (Fig. 8, 3a). Sample CR-01 had a least two exit defects through the frontal bone and involving the orbits (Fig. 8, 2a). In sample SK-01, approximately 75 % of the defect was outlined in dark blue, particularly the inferior half, with lighter blue and green areas surrounding the remainder (Fig. 8, 1a). A similar pattern was observed in sample SK-02, where the lower half of the defect was dark blue, and the upper half was light blue (Fig. 8, 3a). The gunshot wound on the viscerocranium of sample CR-01 was fully outlined in dark blue, with a small bright red area above the left orbit indicating a deviation from the skeletal counterpart (Fig. 8, 2a).

A notable observation from the colour maps of the posterior crania revealed a prominent discrepant ring encircling the lambda for both SK-01 and SK-02 (Fig. 8, 1b and 3b), and just below the lambda for CR-01 (Fig. 8, 2b). This ring appeared red in SK-01 and SK-02 (Fig. 8, 1b and 3b), while CR-01 displayed light blue/green (Fig. 8, 2b). In contrast, SK-03 showed a distinct straight line separating the right side of the sagittal suture from the middle and left side of the cranial vault, delineating dark blue on the right side and light blue on the middle and left sides (Fig. 8, 4b).

The right and left sides of the colour maps exhibited patterns like the viscerocranium, but with localised discrepancies. In SK-01, the left and right mastoids showed green and green with red, respectively, and the left ascending ramus of the mandible appeared green. Specimen CR-01 displayed discrepancies on the right mastoid and maxillary teeth, while SK-02 showed light blue-green on the left mastoid, and SK-03 revealed green on the left side of the viscerocranium, including the left set of teeth and the left maxilla.

When viewed superiorly, specimen SK-01 exhibited the highest level of discrepancy, with green zones on the right side and left parietal bone, surrounded by light blue areas (Fig. 9, 1c). Specimen CR-01 had a

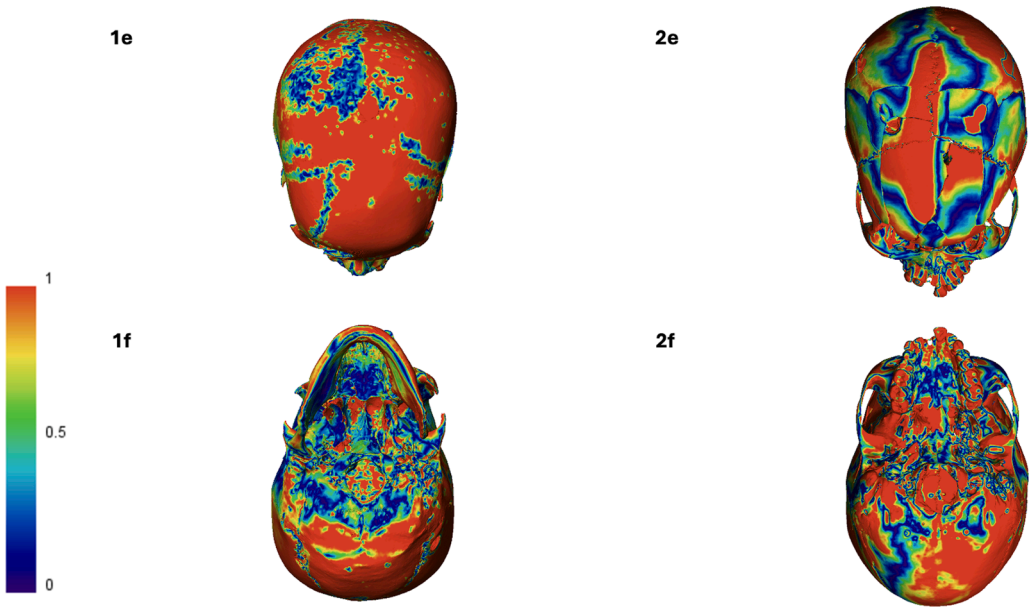

Fig. 7. e) Superior and f) inferior views of the colour maps displaying the discrepancies between samples 1) SK-01 and 2) CR-01, and their respective resin prints. The colour map scale on the left indicates the level of discrepancy shown on the print in millimetres.

smaller light blue area on the right parietal above the entry defect, and a distinct straight line dividing the left frontal and parietal bones, separating dark blue from light blue (Fig. 9, 2c). SK-02 showed green across the right side and light blue on part of the left parietal (Fig. 9, 3c). SK-03 was predominantly light blue, with dark blue on the left parietal and a dark blue area on the bregma (Fig. 9, 4c).

When viewed inferiorly, the samples exhibited scattered light blue and green areas. SK-02 displayed green across the lower mandible (Fig. 9, 3d), CR-01 showed green on the left maxillary teeth (Fig. 9, 2d), and SK-03 mostly presented dark blue, except for the maxillary teeth, which were predominantly green with hints of dark blue and red (Fig. 9, 4d).

Entry defects were identified in SK-01 on the inferior portion of the left parietal bone, in CR-01 on the right parietal, in SK-02 over the right orbital on the frontal bone and the left parietal, and in SK-03 at the suture between the right temporal and sphenoid bones. These were all outlined in dark blue and surrounded by similar hues, except for SK-02, where the superior half of the entry gunshot wound was light blue (Fig. 8, 3a).

Exit defects were observed in SK-01 over the right orbital on the frontal bone (Fig. 8, 1a), and in SK-02 between the left sphenoid, frontal, and left parietal bones, and on the right side of the occipital bone, just posteriorly to the foramen magnum. CR-01 also displayed a fracture on the frontal bone above the orbits, likely resulting from an exit defect (Fig. 8, 2a), similar to the left side of SK-03. These radiating fractures and defects were outlined and surrounded by dark blue, except for the superior half of the exit defect in SK-01 (Fig. 8, 1a) and a small red speck over the left orbit in CR-01 (Fig. 8, 2a). The SK-03 exit fracture exhibited light blue and dark blue outlines, surrounded by dark blue superiorly to the missing bone and lighter blue inferiorly.

Overall, the 3D mesh of specimen SK-01 exhibited the least similarity to its reference mesh, followed by SK-02, CR-01, and SK-03.

3.4. Same specimen prints comparison

A comparison was made between the 3D model mesh accuracy across the three printing technologies (PLA filament, resin, and powder) for samples SK-01 and SK-02. No consistent pattern emerged in the discrepancies observed across the colour maps for the 3D model meshes, except for the following observations:

For specimen SK-01 (Fig. 10), the powder print and PLA print complemented each other. Specifically, when analysing the colour map from a superior view, the green areas of the colour map displaying the discrepancies between the sample and its respective powder 3D print, which corresponded to increased discrepancies, corresponded to regions on the PLA 3D print model with reduced discrepancies, displaying increased green and dark blue levels. Additionally, similarities were noted between the resin and PLA filament prints for this specimen, particularly on the left side, where both exhibited comparable distributions of areas with minimal discrepancies.

Specimen SK-02 (Fig. 11) was printed using both powder and PLA filament. The only discernible pattern was observed on the left profile, where discrepancies were noted. Specifically, the left mastoid and left zygomatic process exhibited increased discrepancies in both prints, with the powder print showing light blue-green areas and the PLA filament print displaying red on the colour maps.

3.5. Intra- and inter-operator reproducibility

Intra- and inter-operator reproducibility testing showed no differences during the colour map analysis within a 1 mm threshold, indicating high reproducibility. These results suggest that any subjectivity during the alignment process did not affect the outcomes.

4. Discussion and future recommendations

Forensic pathologists and anthropologists are responsible for analysing and interpreting bone trauma. Yet, substantiated cases for teaching remain scarce worldwide, especially at the undergraduate and postgraduate levels in the forensic sciences. Additionally, ethical regulations governing the use of skeletal material vary globally, restricting the collection and utilisation of biological materials in educational and legal contexts. As a result, practitioners, law enforcement, and students often lack access to clear, illustrative examples or reliable references of bone trauma. This scarcity makes applying theoretical knowledge to practical bone trauma analysis a challenging endeavour. The application of 3D printing technology in forensic anthropology addresses many of the challenges associated with the use of skeletal material in forensic investigations.

A comparative analysis of colour maps revealed that SLS powder

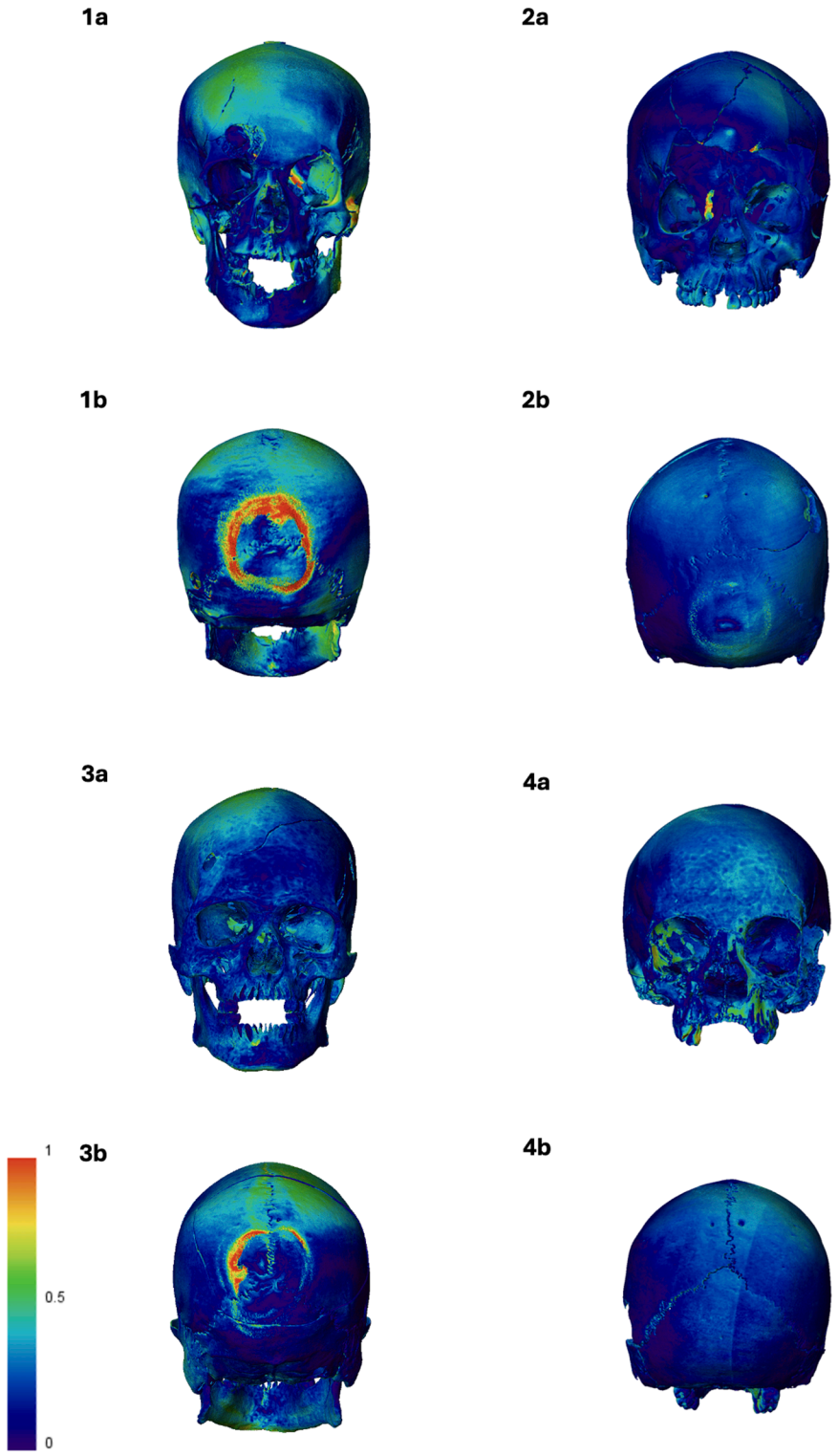

Fig. 8. a) Anterior and b) posterior views of the colour maps displaying the discrepancies between samples 1) SK-01, 2) CR-01, 3) SK-02, and 4) SK-03 and their respective powder prints. The colour map scale on the left indicates the level of discrepancy shown on the print in millimetres.

prints exhibited the fewest discrepancies and, therefore, presented the highest accuracy among the technologies used in this study. While micro-XCT scans offer a higher resolution than CT scans, our findings align with the trends reported by Carew, Morgan, and Rando [20], who 3D-printed skeletal models from CT scans using different technologies. Despite their higher cost for printing and sustainability [21], powder-based prints provided a strong visual resemblance to skeletal material. Moreover, SLS powder-based prints do not require additional support structures during printing, as the powder surrounding the print offers the necessary support [22]. This feature minimised any potential risk of damage during support removal and has already been used in forensic cases, such as a case of blunt force trauma to the head in Poland for analysis [23]. Indeed, unlike the resin used for the SLA prints, the powder does not need to be cured after printing, which avoids any

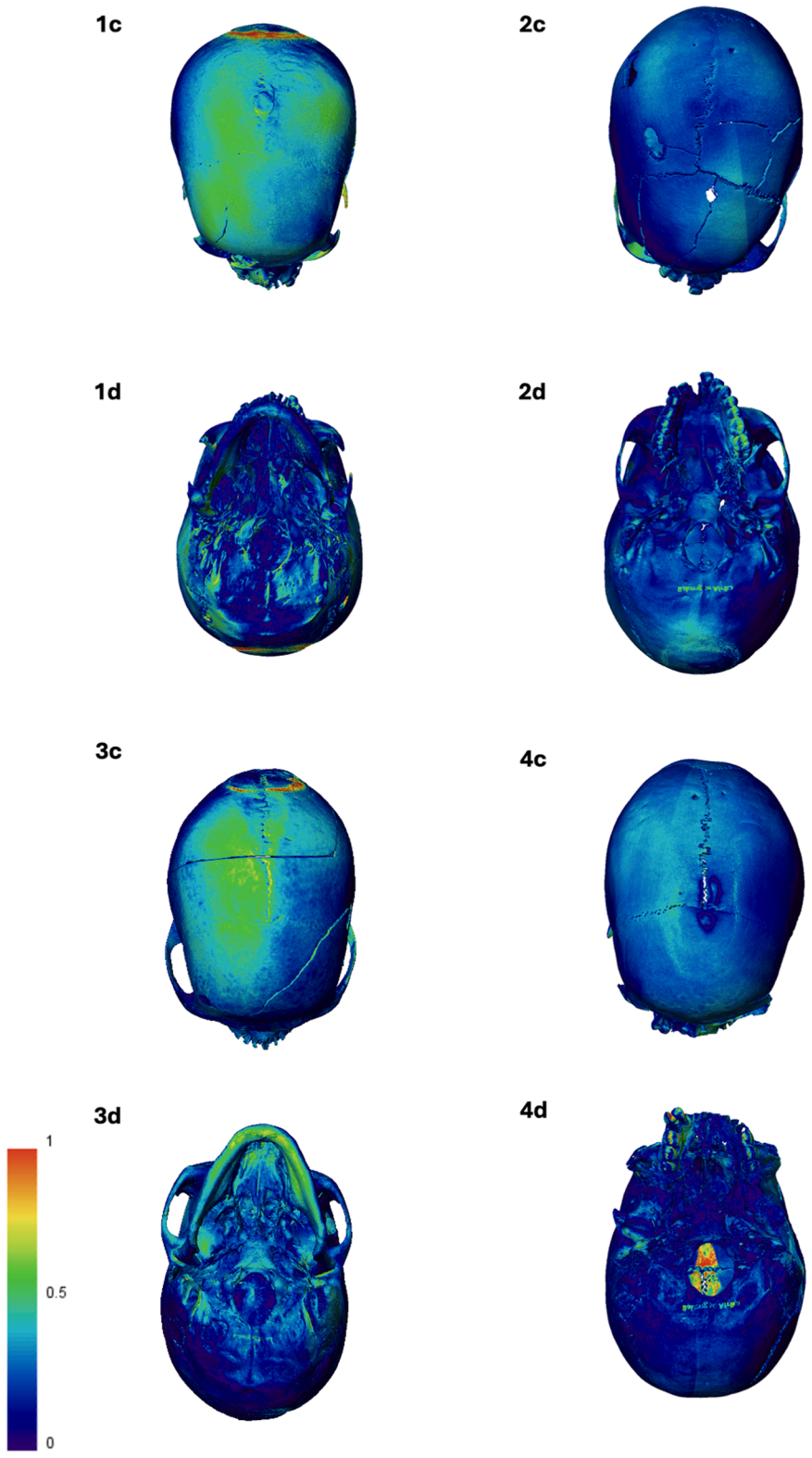

Fig. 9. c) Superior and d) inferior views of the colour maps displaying the discrepancies between samples 1) SK-01, 2) CR-01, 3) SK-02, and 4) SK-03 and their respective powder prints. The colour map scale on the left indicates the level of discrepancy shown on the print in millimetres.

deformation during support removal in case of an unfinished curing process. Additionally, the risk of leaving support fixture points or support structures in unreachable areas will be avoided, which is not the case for SLA resin and FDM PLA filament prints.

FDM PLA filament prints, while easily affordable and accessible, displayed significant discrepancies and defects, such as layer adhesion failure "spaghetti" patterns [24]. Despite judges/jury members and students being able to identify such defects, these can cause problems, particularly near entry or exit defects, potentially altering perceived bullet trajectories or other areas of interest. Additionally, "warping" defects, likely due to printing speed or nozzle height [25], were observed in sample SK-02. These defects were occasionally highlighted

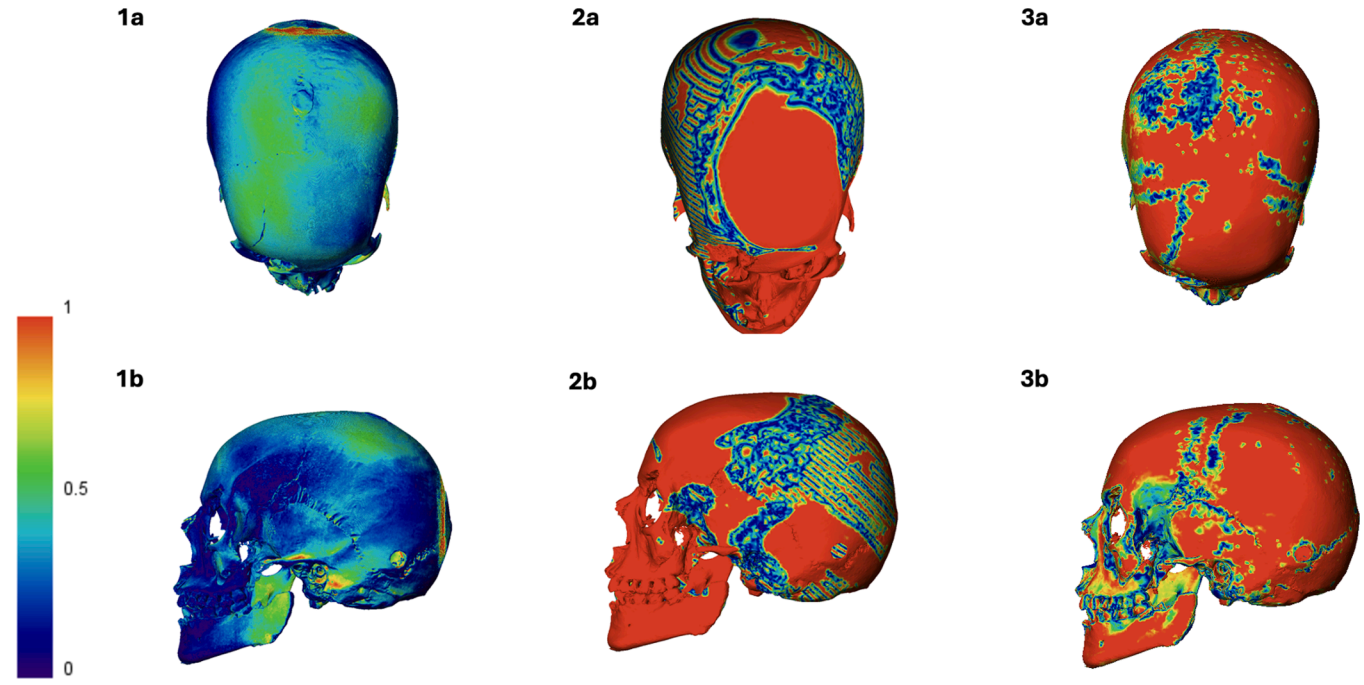

Fig. 10. a) Superior and b) left side views of the colour maps displaying the discrepancies between the sample SK-01 and its respective 1) powder, 2) PLA filament, and 3) resin prints. The colour map scale on the left indicates the level of discrepancy shown on the print in millimetres.

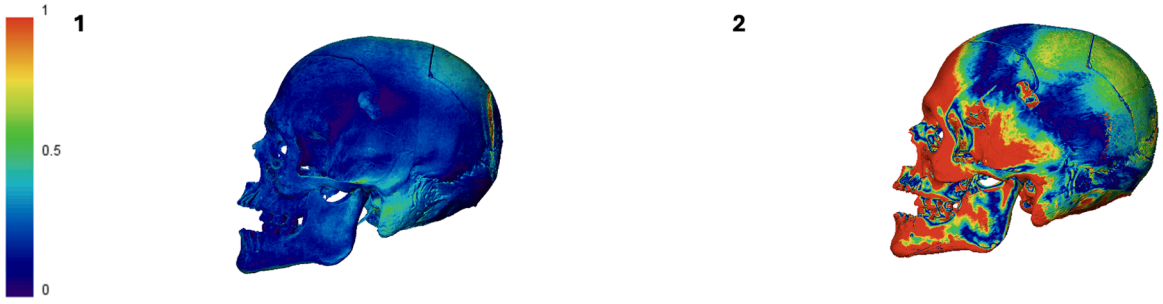

Fig. 11. Left side view of the colour maps displaying the discrepancies between the sample SK-02 and its respective 1) powder, and 2) PLA filament prints. The colour map scale on the left indicates the level of discrepancy shown on the print in millimetres.

in dark blue, indicating their proximity to the actual placement of the bone. Moreover, the weight of new layers on warm and, therefore, flexible lower layers may also lead to deformations in the print [26]. Technical issues, such as missing pieces in the SLA resin prints and layer adhesion failure defects in the FDM PLA filament prints, were noted but did not detract from the overall appearance of the print.

Although SLA resin prints provide better resolution than FDM PLA prints [27], they showed noticeable deformities, including missing pieces and sunken areas. For instance, sample CR-01 displayed small round holes on the occipital and left zygomatic bones, identified as drainage holes for resin [28]. These features should be accounted for in court presentations to prevent confusion with foramina or other anatomical features absent from the skeletal element, and they should also be placed further away from the areas of interest. Furthermore, a large triangular section was missing from the right parietal bone. This anomaly, however, was not observed when using a different material for the same sample or in other 3D prints from the same printer and was, therefore, ruled out as being caused by printer malfunction. However, this defect is likely the result of a small solid piece of resin detaching and falling during the printing process. This is thought to have blocked the laser and prevented subsequent layers from forming. While support structures are added to prevent unsupported areas, skeletal models are complex, and some may have been overlooked. Observed sunken areas in the SLA resin prints may also have resulted from inadequate UV curing, as the UV chamber available was too small for the prints, and therefore, natural sunlight was used instead. Although overexposure to UV light can be detrimental, underexposure can cause deformations [29], such as the indentation observed on the superior part of the CR-01 print, possibly impacting its presentation as evidence.

FDM PLA filament and SLA resin prints require support structures during printing, but their removal processes differ significantly. PLA filament supports are rigid and challenging to remove, while resin supports are more flexible but may leave a rough surface [30,31]. For example, in sample SK-01, a lattice support system was used, which, despite its flexibility, left substantial remnants inside the cranial vault. The manual removal of supports can be time-consuming and risks damaging delicate structures, especially when appropriate tools are unavailable. Furthermore, excessive support structures can overload segmentation software, increasing processing times and potentially causing software failures. Future studies could mitigate these issues in FDM PLA filament prints by using water-soluble materials for the support structures [32].

No specific pattern emerged when comparing colour maps from different print technologies for the same specimen using a maximum

discrepancy of 1 mm. This suggests that the observed discrepancies were more influenced by printer calibration and mesh interpretation than by the 3D model's inherent complexity. While colour maps provide a visual assessment of morphological discrepancies, the study did not include quantitative measurements such as mean, median, or maximum deviations. Therefore, conclusions were limited to visual inspection. Despite this limitation, the colour maps offered a consistent method for comparing morphological discrepancies across samples and materials. Future studies could elaborate on these findings with quantitative data to provide a more rigorous evaluation of morphological accuracy. Additionally, although manual placement of the anatomical landmarks may introduce some subjectivity, despite following the standardised criteria by Caple and Stephan [18], this step was solely used for alignment purposes, and reproducibility testing confirmed that it did not affect the colour map analysis.

Three-dimensional printing technology offers a valuable tool for enhancing the understanding and interpretation of gunshot defects in bone, particularly for judges, students, and the public. A 3D print allows for detailed examination and physical manipulation of evidence, making it highly effective for forensic analysis, courtroom presentations, and educational purposes. In replicating skeletal trauma, 3D prints may provide an objective and reproducible alternative to traditional evidence [33,34].

3D-printed skeletal elements have already been used in court, with evidence from cases involving cranium injuries and fractures [10]. Studies have validated the use of 3D-printed fractures and knife cuts on pig bones using similar technologies as in this study, namely SLA resin and an unspecified FDM filament [12], as well as skull SLS prints in Germany [35]. In cases where skeletal material is needed after burial or cremation, exhumation or loss of evidence becomes a concern. The use of 3D scans, allowing 3D prints to be made, would address these issues and prevent them in future cases. 3D prints used in court could demonstrate the bullet trajectory using a laser pointer [8] and allow the people involved in the verdict to physically manipulate the printed area of interest without the sensory aspects of skeletal evidence [3].

This study determined that despite their higher cost, SLS powder 3D prints provide the highest accuracy and are the most suitable for courtroom evidence and educational purposes. They excel in depicting critical features, such as entry and exit wound defects, making them highly reliable for forensic applications. Carew et al. [20] further support the superior accuracy of SLS powder 3D prints. They evaluated various 3D printing materials for bone replication and concluded that SLS powder 3D printing offers the most precise and visually effective results.

In comparison, FDM PLA filament and SLA resin prints demonstrated high accuracy for specific features but were generally less reliable overall. Notably, improvements in the accuracy of FDM PLA prints when assessing smaller sections may also extend to SLA resin prints. For instance, in a homicide case, an SLA resin-printed skull section was successfully used in court to illustrate forensic evidence [5]. Additionally, subdividing a cranium into smaller sections for resin printing enhances the accuracy significantly, as evidenced by previous research [20].

By tailoring the printing method to the specific requirements of forensic and educational contexts, 3D printing technologies offer versatile and effective solutions for presenting skeletal evidence. Three-dimensional printing offers advantages for forensic analysis, allowing the creation of multiple prints from a single mesh, which can be crucial for fragile or damaged bones. Forensic applications with ballistic trauma to bone often include describing the trajectory in the cranium and, if possible, establishing the sequence of shots [36,37]. The use of powder prints is recommended for accuracy, but FDM PLA filament prints can be suitable for specific regions as they present minimal discrepancies in cranial sections.

The maximum allowed discrepancy was set at 1 mm, which appeared as red on the colour map. Consequently, any larger discrepancies would also appear red and would not be distinguishable from 1 mm deviations. Expanding the threshold for maximum allowable discrepancies in the creation of colour maps could provide a more informative view of the actual maximum discrepancies. Henningsen et al. [9] reported that non-experts considered small discrepancies as irrelevant if the area in question was explained, and that simplified prints did not impact expert testimony. Therefore, despite potential minor discrepancies, 3D prints can still support court cases when accompanied by clear explanations. However, the acceptable threshold may depend on the application. Less accurate SLA resin or FDM PLA filament prints may be sufficient for explaining broader anatomical concepts to a non-expert audience, but more accurate SLS powder prints may be preferred when demonstrating a projectile trajectory. Outside of court use, forensic casework might also benefit from high-accuracy SLS powder prints, particularly if the original remains are unavailable (e.g., reopened cases of buried or cremated remains) or too fragile to perform accurate measurements and assessments, especially regarding projectile trauma. Future studies should further evaluate scenario-dependent thresholds.

Ethical considerations are crucial, particularly regarding the use of 3D prints in cold cases, as this involves consent for handling and using human remains [38]. Standardised country-specific procedures need to be created for the scanning, storage, and printing of skeletal material. All skeletal remains and their associated 3D models should be anonymised. In their ethical framework, Carew, French, and Morgan [39] highlighted nine principles to be applied when using 3D-printed human remains in crime reconstruction. When used as evidence in court, the principles to focus on should be justice, transparency, proportionality, and beneficence. Educational applications of 3D prints include teaching and training, where they can substitute for actual skeletal material and offer advantages in cost and safety [40,41]. The choice of printing technology, FDM, SLS, or SLA, does not appear to impact the effectiveness of the prints in teaching [42]. For their use in education, the remaining principles, anonymity, context, non-maleficence, consent, and autonomy, should remain the focus [39].

5. Conclusion

The frequent discovery of decomposed and skeletonised remains necessitates the application of forensic anthropological methods, which can provide crucial evidence for legal proceedings. However, the use of skeletal evidence in court faces scrutiny due to potential psychological effects that may influence judicial outcomes.

The rising use of 3D printing in forensic anthropology offers potential benefits, such as reducing the exposure of people to biological material, the damage to that material, and the psychological effects of working with human remains. SLS powder-based 3D prints showed higher accuracy levels for whole skulls and crania when comparing the 3D print meshes to their respective reference mesh. With SLS powder-based 3D prints, no noticeable deviations were observed from the reference bone.

FDM PLA filament 3D prints were less accurate for whole skulls and crania. Nonetheless, FDM PLA filament prints demonstrated high morphological accuracy in smaller areas, such as cranial sections with ballistic defects, making them a viable option in some cases due to their greater availability and lower cost. SLA resin 3D prints were the least accurate for whole skulls and crania, and often displayed deformations visibly on the prints.

Understanding the impact of 3D prints on legal verdicts is essential for evaluating their effectiveness in forensic contexts. Future research is therefore needed on how the use of 3D-printed cranial projectile trauma, particularly when accompanied by colour maps, affects judicial decision-making and whether these tools can replace original skeletal material in court. Expanding the parameters for maximum allowable discrepancies in the creation of colour maps and studying the accuracy of different printers for each 3D printing material would help establish standards for legal applications, ensuring their reliability and admissibility.

CRediT authorship contribution statement

Claudia Ibáñez Martín: Writing – review & editing, Writing – original draft, Visualization, Validation, Software, Project administration, Investigation, Funding acquisition, Formal analysis, Data curation. **Ericka Noelle L'Abbé:** Writing – review & editing, Supervision, Resources, Project administration, Methodology, Conceptualization. **Pieter Daniël de Wet:** Writing – review & editing, Validation, Software, Investigation, Formal analysis, Data curation. **Alison Fany Ridel:** Writing – review & editing, Validation, Supervision, Software, Resources, Project administration, Methodology, Data curation, Conceptualization.

Declaration of competing interest

The authors declare the following financial interests/personal relationships which may be considered as potential competing interests:

Claudia Ibáñez Martín reports financial support was provided by Amsterdam University Fund. If there are other authors, they declare that they have no known competing financial interests or personal relationships that could have appeared to influence the work reported in this paper.

Acknowledgements

We want to express our deepest gratitude to Mr. Marius Loots[a] for providing the 3D prints, which were essential for the completion of this study. We are also grateful to the engineers at NECSA, Dr. Lunga Bam[b] and Mr. Jakobus Hoffman[b], for handling the Micro-XCT scanning. Additionally, we thank Dr. A.E. (Lida) Van der Merwe[c] for her participation and guidance during the MSc project which ultimately led to the development of this paper.

[a] Department of Anatomy, University of Pretoria, Private Bag x323, 0007, Arcadia, South Africa

[b] Department of Radiation Science, South African Nuclear Energy Corporation (NECSA), Pretoria 0001, South Africa

[c] Department of Medical Biology, Amsterdam University Medical Centre, Location AMC, University of Amsterdam, Amsterdam, The Netherlands

References

[1] A. Karp, Estimating global civilian-held firearms numbers. Briefing Paper, Small Arms Survey, Geneva, Switzerland, 2018.

[2] D.A. Komar, S. Davy-Jow, S.J. Decker, The use of a 3-D laser scanner to document ephemeral evidence at crime scenes and postmortem examinations, J. Forensic Sci. 57 (1) (2012) 188–191, https://doi.org/10.1111/j.1556-4029.2011.01915.x.

[3] K.F. Peterson, Enhanced persuasion: effective use of demonstrative evidence at trial, J. Consum. Attorney.Assoc. South. Californ. Adv. 37 (2010) 1–5.

[4] S. Blau, E. Phillips, C. O'Donnell, G. Markowsky, Evaluating the impact of different formats in the presentation of trauma evidence in court: a pilot study, Austral. J. Forensic Sci. 51 (6) (2019) 695–704, https://doi.org/10.1080/00450618.2018.1457717.

[5] W. Baier, J.M. Warnett, M. Payne, M.A. Williams, Introducing 3D printed models as demonstrative evidence at criminal trials, J. Forensic Sci. 63 (4) (2018) 1298–1302, https://doi.org/10.1111/1556-4029.13700.

[6] R.M. Carew, J. French, R.M. Morgan, Suitability of 3D printing cranial trauma: prospective novel applications and limitations of 3D replicas, Forensic Sci. Int.: Rep. 4 (2021) 100218, https://doi.org/10.1016/j.fsir.2021.100218.

[7] D. Errickson, H. Fawcett, T.J.U. Thompson, A. Campbell, The effect of different imaging techniques for the visualisation of evidence in court on jury comprehension, Int. J. Legal. Med. 134 (2020) 1451–1455, https://doi.org/10.1007/s00414-019-02221-y.

[8] R.M. Carew, D. Errickson, An overview of 3D printing in forensic science: the tangible third-dimension, J. Forensic Sci. 65 (5) (2020) 1752–1760, https://doi.org/10.1111/1556-4029.14442.

[9] M.J. Henningsen, L. Thorlacius-Ussing, L.G. Jensen, K. Hansen, C. Jacobsen, S. Lou, C. Villa, 3D printed skulls in court—A benefit to stakeholders? Int. J. Legal. Med. 137 (6) (2023) 1865–1873, https://doi.org/10.1007/s00414-023-03054-6.

[10] D. Errickson, R.M. Carew, A.J. Collings, M.J.P. Biggs, P. Haig, H. O'Hora, N. Marsh, J. Roberts, A survey of case studies on the use of forensic three-dimensional printing in England and Wales, Int. J. Legal. Med. 136 (6) (2022) 1605–1619, https://doi.org/10.1007/s00414-022-02872-4.

[11] Y. AbouHashem, M. Dayal, S. Savanah, G. Štrkalj, The application of 3D printing in anatomy education, Med. Educ. Online 20 (1) (2015) 29847, https://doi.org/10.3402/meo.v20.29847.

[12] W. Baier, D.G. Norman, M.J. Donnelly, M.A. Williams, Forensic 3D printing from micro-CT for court use-process validation, Forensic Sci. Int. 318 (2021) 110560, https://doi.org/10.1016/j.forsciint.2020.110560.

[13] A.J. Arockiam, K. Subramanian, R.G. Padmanabhan, R. Selvaraj, D.K. Bagal, S. Rajesh, A review on PLA with different fillers used as a filament in 3D printing, Mater. Today: Proceed. 50 (2022) 2057–2064, https://doi.org/10.1016/j.matpr.2021.09.413.

[14] B. Evans, Practical 3D printers: The science and art of 3D printing, Apress, 2012.

[15] S.H. Huang, P. Liu, A. Mokasdar, L. Hou, Additive manufacturing and its societal impact: a literature review, Int. J. Adv. Manufact. Technol. 67 (2013) 1191–1203, https://doi.org/10.1007/s00170-012-4558-5.

[16] C.A. Schneider, W.S. Rasband, K.W. Eliceiri, NIH image to ImageJ: 25 years of image analysis, Nat. Method. 9 (7) (2012) 671–675, https://doi.org/10.1038/nmeth.2089.

[17] C.F. Spoor, F.W. Zonneveld, G.A. Macho, Linear measurements of cortical bone and dental enamel by computed tomography: applications and problems, Am. J. Phys. Anthropol. 91 (4) (1993) 469–484, https://doi.org/10.1002/ajpa.1330910405.

[18] J. Caple, C.N. Stephan, A standardized nomenclature for craniofacial and facial anthropometry, Int. J. Legal. Med. 130 (3) (2016) 863–879, https://doi.org/10.1007/s00414-015-1292-1.

[19] F.P. Yean, W.J. Chew, Detection of spaghetti and stringing failure in 3D printing, in: 2024 International Conference on Green Energy, Computing and Sustainable Technology (GECOST), IEEE, 2024, pp. 293–298, https://doi.org/10.1109/GECOST60902.2024.10475059.

[20] R.M. Carew, R.M. Morgan, C. Rando, A preliminary investigation into the accuracy of 3D modeling and 3D printing in forensic anthropology evidence reconstruction, J. Forensic Sci. 64 (2) (2019) 342–352, https://doi.org/10.1111/1556-4029.13917.

[21] L. Carolo, *3D printer material cost of 2023*. All3DP, Retrieved May 24, 2024, from, https://all3dp.com/2/3d-printer-material-cost-the-real-cost-of-3d-printing-materials/#i-16-metals, 2023.

[22] G. Brunello, S. Sivolella, R. Meneghello, L. Ferroni, C. Gardin, A. Piattelli, B. Zavan, E. Bressan, Powder-based 3D printing for bone tissue engineering, Biotechnol. Adv. 34 (5) (2016) 740–753, https://doi.org/10.1016/j.biotechadv.2016.03.009.

[23] K. Woźniak, E. Rzepecka-Woźniak, A. Moskała, J. Pohl, K. Latacz, B. Dybała, Weapon identification using antemortem computed tomography with virtual 3D and rapid prototype modeling—a report in a case of blunt force head injury, Forensic Sci. Int. 222 (1–3) (2012) e29–e32, https://doi.org/10.1016/j.forsciint.2012.06.012.

[24] H. Kim, H. Lee, S.H. Ahn, Systematic deep transfer learning method based on a small image dataset for spaghetti-shape defect monitoring of fused deposition modeling, J. Manuf. Syst. 65 (2022) 439–451, https://doi.org/10.1016/j.jmsy.2022.10.009.

[25] Z. Jin, Z. Zhang, G.X. Gu, Autonomous in-situ correction of fused deposition modeling printers using computer vision and deep learning, Manuf. Lett. 22 (2019) 11–15, https://doi.org/10.1016/j.mfglet.2019.09.005.

[26] J. Suder, Z. Bobovsky, M. SAFAR, J. Mlotek, M. Vocetka, Z. ZEMAN, Experimental analysis of temperature resistance of 3D printed PLA components, MM Sci. J. (2021), https://doi.org/10.17973/MMSJ.2021_03_2021004.

[27] G. Jani, A. Johnson, J. Marques, A. Franco, Three-dimensional (3D) printing in forensic science–An emerging technology in India, Annal. 3D Print. Med. 1 (2021) 100006, https://doi.org/10.1016/j.stlm.2021.100006.

[28] M. Idris, T.D. Seers, N. Alyafei, An operational guide to resin 3D printing of geological macromodels, MethodsX. 9 (2022) 101863, https://doi.org/10.1016/j.mex.2022.101863.

[29] C. Lannon, Overcoming common resin 3D printing curing issues, Mach5ive (2023). Retrieved November 15, 2024, from, https://mach5ive.com/blogs/learning-center/overcoming-common-resin-3d-printing-curing-issues.

[30] C. Arnold, D. Monsees, J. Hey, R. Schweyen, Surface quality of 3D-printed models as a function of various printing parameters, Materials 12 (12) (2019) 1970, https://doi.org/10.3390/ma12121970.

[31] N. Zhang, L.C. Zhang, Y. Chen, Y.S. Shi, Local barycenter based efficient tree-support generation for 3D printing, Comput.-Aid. Des. 115 (2019) 277–292, https://doi.org/10.1016/j.cad.2019.06.004.

[32] M. Engli Rueda, N.A. Gomez, G.M. Navarro, J.M. del Cerro, A. Valls Esteve, Soluble vs non-Soluble support materials for bone 3D printed anatomical models: a comparison on production time, cost and finish quality, Key. Eng. Mater. 958 (2023) 13–20, https://doi.org/10.4028/p-0eVVHy.

[33] H.E. Berryman, A systematic approach to the interpretation of gunshot wound trauma to the cranium, Forensic Sci. Int. 301 (2019) 306–317, https://doi.org/10.1016/j.forsciint.2019.05.019.

[34] C.L. Humphrey, Characterisation of soft tissue and skeletal bullet wound trauma and three-dimensional anatomical modelling, The University of Adelaide, 2017. PhD thesis.

[35] M. Kettner, P. Schmidt, S. Potente, F. Ramsthaler, M. Schrodt, Reverse engineering—Rapid prototyping of the skull in forensic trauma analysis, J. Forensic Sci. 56 (4) (2011) 1015–1017, https://doi.org/10.1111/j.1556-4029.2011.01764.x.

[36] B. Madea, M. Staak, Determination of the sequence of gunshot wounds of the skull, J. Forensic Sci. Soc. 28 (5–6) (1988) 321–328, https://doi.org/10.1016/S0015-7368(88)72858-3.

[37] P. Mahoney, D. Carr, R. Arm, I. Gibb, N. Hunt, R.J. Delaney, Ballistic impacts on an anatomically correct synthetic skull with a surrogate skin/soft tissue layer, Int. J. Legal. Med. 132 (2018) 519–530, https://doi.org/10.1007/s00414-017-1737-9.

[38] E.N. L'Abbé, A. Alblas, J.H.P. Ackermann, L. Bam, A. Beaudet, P.N. Bothma, A. Carmichael, M. Cazenave, E. Cunha, F. de Beer, E. de Jager, M.-K. Erasmus, A.C. Hagg, M. Harripershad, P.C. Hartman, Y. Heuzé, J. Hoffman, N. Japhta, R. Khonyane, R. Kobedi,Gabriele C. Krüger, Maritza Liebenberg, Leandi Liebenberg, Marius Loots, Chantelle Marais, Thandolwethu Mbonani, Michaela Middleton, Samantha Muller, Robert Nshimirimana, Anna C. Oettlé, Rachel Pieterse, Alison F. Ridel, Okuhle Sapo, Franci Swanepoel, Charlotte E. G. Theye, Clarisa van der Merwe, Dirk Vandermeulen, R. Venter, Bakeng se Afrika: digital skeletal repository: advancing biological anthropology and medical research in South Africa, in: L. Shapiro (Ed.), How to use 3D printing innovations and digital storage to democratize anatomy education, Springer, 2024, pp. 63–75, 10.1007/978-3-031-68501-9_3.

[39] R.M. Carew, J. French, R.M. Morgan, An ethical framework for the creation and use of 3D printed human remains in crime reconstruction, Forensic Sci. Int.: Rep. 7 (2023) 100319, https://doi.org/10.1016/j.fsir.2023.100319.

[40] A.M. Wu, K. Wang, J.S. Wang, C.H. Chen, X.D. Yang, W.F. Ni, Y.Z. Hu, The addition of 3D printed models to enhance the teaching and learning of bone spatial anatomy and fractures for undergraduate students: a randomized controlled study, Ann. Transl. Med. 6 (20) (2018) 403, https://doi.org/10.21037/atm.2018.09.59.

[41] S. Youman, E. Dang, M. Jones, D. Duran, B. Brenseke, The use of 3D printers in medical education with a focus on bone pathology, Med. Sci. Educ. 31 (2021) 581–588, https://doi.org/10.1007/s40670-021-01222-0.

[42] A. Pandžić, D. Hodžić, A. Milovanović, Effect of infill type and density on tensile properties of PLA material for FDM process, in: Proceedings of the 30th DAAAM International Symposium, DAAAM International, 2019, pp. 545–554, https://doi.org/10.2507/30th.daaam.proceedings.074.